

LETTER TO THE EDITOR

Discovery of a PRS associated with FRB 20240114A

G. Bruni¹, L. Piro¹, Y.-P. Yang^{2,3}, E. Palazzi⁴, L. Nicastro⁴, A. Rossi⁴, S. Savaglio^{5,4,6}, E. Maiorano⁴, and B. Zhang^{7,8}

¹ INAF – Istituto di Astrofisica e Planetologia Spaziali, via Fosso del Cavaliere 100, 00133 Rome, Italy
e-mail: gabriele.bruni@inaf.it

² South-Western Institute for Astronomy Research, Yunnan University, Kunming, China.

³ Purple Mountain Observatory, Chinese Academy of Sciences, Nanjing, China.

⁴ INAF – Osservatorio di Astrofisica e Scienza dello Spazio di Bologna, via Piero Gobetti 93/3, I-40129 Bologna, Italy

⁵ Dipartimento di Fisica, Università della Calabria, Arcavacata di Rende, Italy

⁶ Laboratori Nazionali di Frascati, INFN (Istituto Nazionale di Fisica Nucleare), Frascati, Italy

⁷ Nevada Center for Astrophysics, University of Nevada, Las Vegas, NV, USA.

⁸ Department of Physics and Astronomy, University of Nevada, Las Vegas, NV, USA

Received November 30, 20XX

ABSTRACT

Aims. We present the discovery of the fourth persistent radio source (PRS) associated with a fast radio burst (FRB).

Methods. Following previous indications of a candidate PRS associated with FRB 20240114A, we performed deep VLBA observations at 5 GHz to test the presence of a compact radio source within the uncertainty position of this FRB (± 200 mas).

Results. We detect a component ~ 50 mas northwards the nominal position provided by the PRECISE collaboration. The corresponding radio luminosity, together with the Faraday rotation measure provided by previous observations of the FRB, locate this PRS in the expected region of the L vs $|RM|$ relation for the nebular model, further supporting it. The comparison of the measured flux density with the respect to the values collected at lower frequency by previous studies, indicates a steepening of the radio spectrum in the 1–3 GHz range and the presence of a possible synchrotron peak at ~ 1 GHz. Optical observations performed with the LBT could reveal that the FRB and its PRS lie at ~ 1 kpc from the centre of the host galaxy, which is a dwarf sub-solar metallicity starburst galaxy with $SFR \sim 1 M_{\odot} \text{ yr}^{-1}$ and stellar mass $M \sim 10^8 M_{\odot}$.

Key words. fast radio bursts – Stars: magnetars

1. Introduction

Fast Radio Bursts (FRBs) are bright millisecond-duration sources of extragalactic origin, so far only observed at radio wavelengths. The vast majority (> 700) are one-off events but several are repeating (rFRBs) (see e.g. Zhang et al. 2023). It is not unlikely that the repeating nature is ubiquitous, but often too faint to be caught (Kirsten et al. 2024). Notwithstanding, the large number of events and the substantial efforts to carry out deep multiwavelength observations, the lack of counterparts at other wavelengths, with one possible exception of a magnetar in our Galaxy (Bochenek et al. 2020), has left the door open for various progenitor models.

Magnetars can reproduce many of the observed properties (Zhang 2020) and are one of the leading scenarios for FRB central engines. However, even this kind of object can be formed by different progenitor channels. For instance, in young (through core-collapse supernovae) or older (through compact binary coalescence) stellar environments (Margalit et al. 2019; Niu et al. 2022), as seen for FRB 20200120E in a globular cluster (Kirsten et al. 2022). Such different progenitors can in principle account for different properties of the host and local environment, but the present sample is still quantitatively and qualitatively limited to settle the issue. An important step forward has been pioneered in the last years by extending the study of the environment from radio to X-rays, including high-resolution optical and IR spectrophotometry, down to the sub arcsec level (Piro et al. 2021; Bruni et al. 2024). This approach has proven to be highly

rewarding, allowing to properly map the star formation in the galaxy and single out the presence of a low luminosity and continuous radio source (persistent radio source, PRS) connected to the central engine in FRB 20201124A (Bruni et al. 2024).

1.1. PRS: the closest environment of FRBs

The discovery of compact PRSs associated with three rFRBs was an important progress in the study of FRB possible progenitors: FRB 20121102A (Chatterjee et al. 2017), FRB 20190520B (Niu et al. 2022) and FRB 20201124A (Bruni et al. 2024). Such a compact emission may hold the key to unveil the central engine. Highly active repeaters could be newborn magnetars still residing in their complex, magnetized, natal environment. The large Faraday rotation $|RM|$ values of some FRBs imply a dense and magnetized environment close to the sources, which led to the idea of a simple relation between the luminosity of the PRS and the $|RM|$, tracing the magneto-ionic medium in the FRB environment (Yang et al. 2020, 2022). If a population of relativistic electrons is maintained within such a magnetised medium, it will naturally produce synchrotron radiation, powering a bright PRS (Murase et al. 2016; Margalit & Metzger 2018). The recent discovery of the PRS associated with FRB 20201124A validate the relation by extending the explored range of RM and Luminosity by two orders of magnitude, and supporting the idea that the persistent radio emission is of nebular origin (Bruni et al. 2024). Moreover, a VLA systematic search towards 37 CHIME repeat-

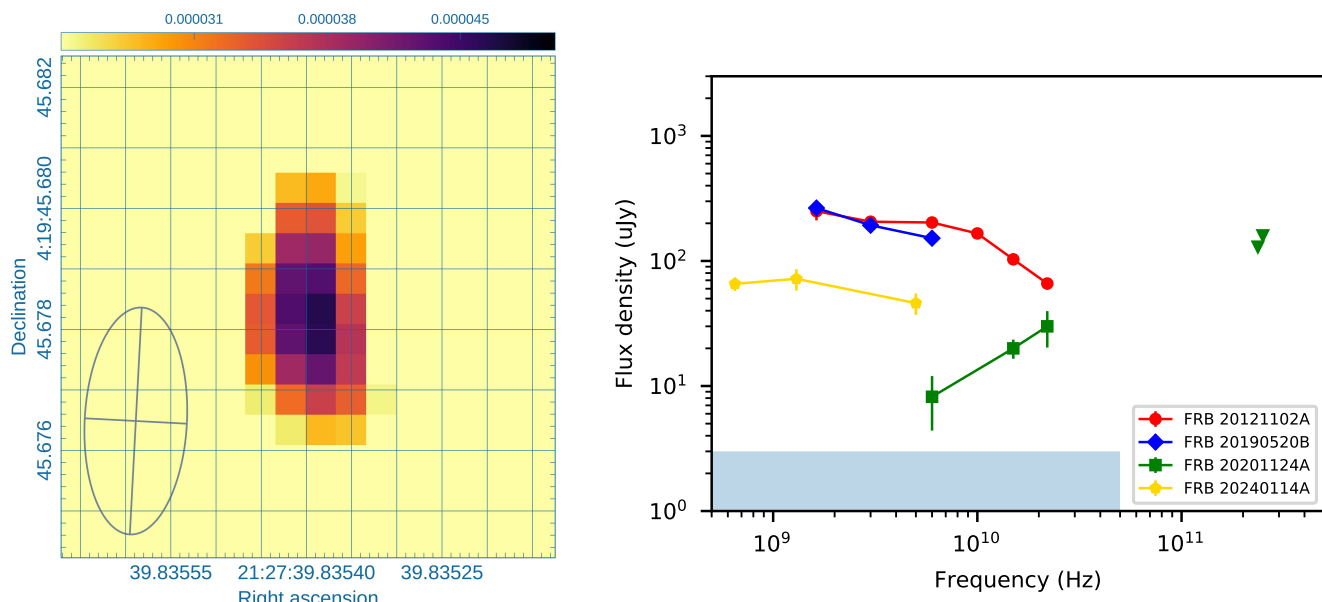


Fig. 1: Left panel: VLBA image of the PRS at 5 GHz. Units are in Jy. The FWHM (3.7×1.7 mas) is shown in the lower-left corner. Pixels below $3\text{-}\sigma$ significance have been blanked. Right panel: radio spectral shape of the four PRS discovered so far, built with VLA data (except for our VLBA 5 GHz measurement). The blue shaded area represents the region below the $3\text{-}\sigma$ VLA sensitivity, in the range 1–50 GHz.

ing FRBs revealed further two candidate PRSs, that fall in the expected region of the luminosity vs $|\text{RM}|$ relation (Ibik et al. 2024). Since nebulae can originate from magnetars and hyperaccreting X-ray binaries, these findings are crucial to disentangle among different scenarios, and eventually circumscribe the nature of the FRB central engine.

2. The hyper active FRB 20240114A

Recently, a further nearby, very active repeating FRB has been found by CHIME/FRB (FRB 20240114A, Shin & CHIME/FRB Collaboration 2024), and associated with a nearby galaxy ($z = 0.13$; Bhardwaj et al. 2024). The localization provided by the PRECISE collaboration through EVN observations of the bursts (Snelders et al. 2024) allowed to lower the uncertainty to ~ 200 mas. Since its discovery, FRB 20240114A had been very active, showing burst rates up to ~ 500 bursts per hour in the 1.0–1.5 GHz band (Zhang et al. 2024).

Further radio continuum observations at \sim arcsec resolution allowed to identify a candidate PRS, first through a reanalysis of MeerKAT data (Zhang & Yu 2024), that detected a continuum emission of $72 \pm 14 \mu\text{Jy}$ at 1.3 GHz, and more recently through uGMRT observations at 650 MHz, that detected a continuum source with a flux density of $65.6 \pm 8.1 \mu\text{Jy}$, suggesting a flat spectrum (Bhusare et al. 2024). Nevertheless, in-band spectral analysis of MeerKAT data resulted in a spectral index of -1.1 ± 0.8 between 1 and 1.5 GHz, suggesting a possible steepening of the radio emission at higher frequencies. However, these observations at a few arcsec resolution did not allow to secure the association with the FRB itself.

3. Confirmation of the associated PRS

During September 2024, we performed e-Merlin and VLBA follow-up observations pointed at the FRB coordinates provided

by the PRECISE collaboration. Details for the VLBA observations are discussed below, while the e-Merlin ones resulted in an upper limit, and are reported in Appendix A. Main quantities are reported in Table 1.

3.1. VLBA detection of a compact radio source

We observed the FRB location with the Very Long Baseline Array (VLBA) at 5 GHz (C-band) under DDT project BB468 (PI Bruni). Observations were divided into two identical runs, on September 28th and 30th, 2024, for a total of 12 hours. Phase referencing was applied. Data were reduced through the standard AIPS procedure for continuum, then calibrated visibilities from the two runs were concatenated and imaged in CASA, achieving an angular resolution of 3.7×1.7 milli-arcsec in natural weighting, and an RMS of $8 \mu\text{Jy}/\text{beam}$.

An unresolved source was identified within the ± 200 mas FRB positional uncertainty provided by the PRECISE collaboration, ~ 50 mas Northwards the phase center (see Fig. 1, left panel). The peak position is RA: 21:27:39.83538, Dec: 04:19:45.6783 (J2000). Image registration is provided by phase-referencing, we thus consider 10% of the FWHM major axis as a conservative estimate of the positional uncertainty, i.e. ± 0.4 mas. The measured flux density (peak) is $46 \pm 9 \mu\text{Jy}$, where the uncertainty is the squared sum of the image RMS plus a typical 10% uncertainty on the absolute flux scale. The ratio between peak and RMS corresponds to a $5.7\text{-}\sigma$ detection. The flux falls below the e-Merlin upper limit at the same frequency. No other statistically significant peak was found in the uncertainty region from PRECISE. At the redshift of the host galaxy, the physical size of the PRS is constrained to $\lesssim 4$ pc. This results in a brightness temperature $T_b > 7.8 \times 10^5$ K, and a luminosity $L_{\text{radio}} = 2.2 \times 10^{28}$ $\text{erg s}^{-1} \text{Hz}^{-1}$, placing the PRS more than one order of magnitude above the luminosity of the brightest star forming regions, and suggesting a non-thermal (synchrotron) origin for its radio emission, consistently with the other PRSs studied so far.

Table 1: Journal of radio observations.

Telescope	Date (dd/mm/yyyy)	Frequency (GHz)	FWHM (mas)	RMS (μ Jy/beam)	Flux density (μ Jy)
e-Merlin	20–28/09/2024	5	228×87	10	< 50
VLBA	28,30/09/2024	5	3.7×1.7	8	46 ± 9

This detection confirms the presence of a compact, continuum source associated with FRB 20240114A, making this the fourth PRS known to date - following FRB 20121102A (Chatterjee et al. 2017), FRB 20190520B (Niu et al. 2022), and FRB 20201124A (Bruni et al. 2024).

3.2. Radio spectrum of the PRS

In Fig. 1, right panel, we show the radio spectrum of the newly discovered PRS together with the other three ones known so far. As discussed in the literature, while the PRS associated with FRB 20121102A and FRB 20190520B showed a negative spectral index, the more recent one found for FRB 20201124A showed a positive, inverted spectral index. The mentioned uGMRT and MeerKAT detections for the PRS of FRB 20240114A suggest a flat/inverted spectrum between 0.65 and 1.3 GHz ($\alpha = 0.13 \pm 0.33$), while the in-band spectrum in MeerKAT data (1–1.5 GHz) indicated a steepening of the spectrum ($\alpha = -1.1 \pm 0.8$). Our VLBA detection further confirms a steepening between 1.3 and 5 GHz ($\alpha = -0.34 \pm 0.21$). However, uGMRT and MeerKAT observations, at a resolution of several arcsec, encompass the whole host galaxy (see Fig. 2), not allowing to disentangle its possible contribution from the emission of the compact PRS. Only further VLBI observations in the 1–2 GHz range would pinpoint the compact PRS emission and correctly estimate its flux density. This would allow a comparison with the MeerKAT flux at the same frequency, and assess the spectral curvature of the PRS: in case the flux density would result consistent with MeerKAT, this would confirm the spectral curvature suggested by the lower flux density at 650 MHz measured by uGMRT, resulting in the first PRS with a peaked synchrotron spectrum. This would make this PRS an intermediate case between the two steep PRS associated with previous FRBs, and the more recent inverted one associated with FRB 20201124A.

4. Host galaxy properties

4.1. Optical observations and SED fitting

Photometric observations of FRB 20240114A were obtained in the $g'r'i'z'$ optical band with the Large Binocular Cameras (LBCs; Giallongo et al. 2008) mounted on the Large Binocular Telescope (LBT) on Mt. Graham, Arizona, USA. Data were collected on November 9th, 2024 and additional ones only in the $r'i'$ on the following night. Data reduction is described in Appendix B. We estimate the galaxy centre to be RA=21:27:39.849, Dec=+04:19:46.00 (J2000) with an extension of $\approx 3''.2 \times 2''.8$ (Fig. 2), corresponding to a physical size of $\approx 7.7 \times 6.7$ kpc for a scale of 2.4 kpc'' at redshift $z = 0.13$. The PRS is located $0''.43$ from the centre of the host galaxy, which corresponds to ≈ 1 kpc.

After correction for the Galactic foreground extinction of $E(B - V) = 0.06$ mags (Schlafly & Finkbeiner 2011), we modeled the spectral energy distribution (SED) of the host galaxy using the Cigale code (Boquien et al. 2019). We added the $u' =$

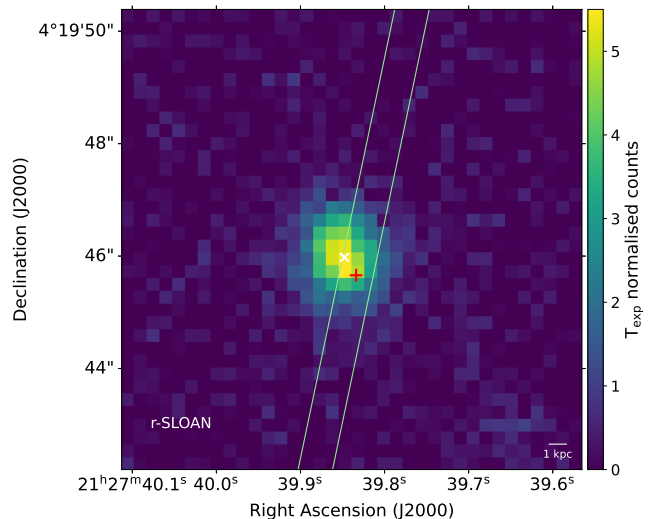


Fig. 2: LBC r' filter image with the PRS position marked by a plus sign and the galaxy centre with a \times . The slit used for the MODS spectrum is shown. The image pixel scale is $0''.23$ and the rms is 0.25 cts. The galaxy extension is $\approx 3''.2 \times 2''.8$.

23.0 ± 0.4 detection from the SDSS survey to our dataset (see Fig. B.1). In addition, we fixed the redshift to 0.13 and used a derived stellar dust attenuation derived from the one measured with the Balmer decrement, $E(B - V)_{\text{star}} = 0.4 \times E(B - V)_{\text{gas}}$ (Calzetti 1997; Asari et al. 2007). The galaxy model gives $\chi^2/\text{dof} = 0.25$ for a stellar mass $M_{\star} = 10^{8.1 \pm 0.2} M_{\odot}$ and star-formation rate $\text{SFR} < 1 M_{\odot} \text{ yr}^{-1}$. While the derived stellar mass is reliable, the SFR is degenerate with age (0.3–1.2 Gyr).

4.2. Spectroscopic observations and data analysis

On November 10th, 2024 a set of 3 spectroscopic exposures of 1200 s each were performed with the Multi-Object Double Spectrograph MODS-1 (Pogge et al. 2010) mounted on LBT. We used the dual-grating mode providing a wavelength coverage of 3200–9500 Å and a slit mask with a width of $1''.2$. The slit was intentionally placed with a position angle of $-11''.9$ and centred on the position of the PRS, therefore not covering the whole galaxy (see Fig. 2). A redshift of $z = 0.13056 \pm 0.00003$ was determined (see Appendix B for the details). By using the dust-corrected fluxes and the prescription provided by Kennicutt (1998) and Savaglio et al. (2009), we derived $\text{SFR}(H\alpha) = 0.36 \pm 0.01 M_{\odot}/\text{yr}$. We note that this is the SFR measured in the region of the galaxy covered by the slit which results to be 40% of the whole galaxy extension. Consequently, the total SFR is likely higher than the measured value, $\text{SFR}(H\alpha) \approx 0.9$. The resulting specific star-formation rate (sSFR) for the entire galaxy is $-8.5 < \log(\text{sSFR}) < -8.1 \text{ yr}^{-1}$, which is one of the highest sSFR value for FRB hosts (see e.g. Nicastro et al. 2021) and it is typical of a galaxy in a "starburst" regime.

We also used the dust corrected line fluxes (see Tab. B.1) to compute the following ratios $[S II]/H\alpha = -0.910 \pm 0.007$, $[N II]/H\alpha = -0.998 \pm 0.003$ and $[O III]/H\beta = 0.498 \pm 0.004$, which places the host galaxy within the star-forming region of the Baldwin-Phillips-Terlevich (BPT, Baldwin et al. (1981) diagram (see Figs. B.3, B.4). To estimate the gas metallicity, we used the method proposed by Curti et al. (2017), which gives an average metallicity from all possible metallicity calibrators. This yielded to $12 + \log(O/H) \sim 8.5$. This metallicity, although sub-solar, is relatively high, if one considers the mass-metallicity relation for galaxies with similar stellar mass at $z \sim 0.1$ (Bassini et al. 2024).

5. Implications for the nebular model

As shown in Fig. 1 (right panel), the SED of the PRS associated with FRB 20240114A is similar to those of the PRSs associated FRB 20121102A and FRB 20190520B. Based on the observed SED, the peak frequency is at $\nu_{\text{peak}} \sim 1$ GHz. The PRS has been proposed to be generated by the synchrotron emission (e.g., Yang et al. 2020), thus, the peak frequency ν_{peak} should correspond to the typical frequency of the synchrotron from the electrons with the minimum Lorentz factor γ_m , leading to

$$\nu_m = \frac{\gamma_m^2 e B}{2\pi m_e c} \sim \nu_{\text{peak}} \sim 1 \text{ GHz} \quad (1)$$

where B is the magnetic field strength at the emission region. Therefore, we obtain the following constraints:

$$\left(\frac{\gamma_m}{10^3}\right)^2 \left(\frac{B}{1 \text{ mG}}\right) \sim 0.36 \quad (2)$$

Yang et al. (2020, 2022) proposed that the RM of an FRB repeater and the associated PRS might originate from the same region. In this case, there is a simple relation between the RM and the PRS luminosity, which is generic and weakly depends on the PRS model. Since the PRS is likely powered by synchrotron radiation due to their non-thermal spectra at radio bands (Yang et al. 2016, 2020, 2022; Murase et al. 2016; Metzger et al. 2017), the PRS brightness will depend on the electron distribution and the parallel strength of local magnetic fields. It has been suggested that $|RM|$ could be a good proxy of the PRS luminosity, with a predicted scaling law of Yang et al. (2020, 2022),

$$L_\nu = \frac{64\pi^3}{27} \zeta_e \gamma_c^2 m_e c^2 R^2 |RM| \approx 5.7 \times 10^{28} \text{ erg s}^{-1} \text{ Hz}^{-1} \zeta_e \gamma_c^2 \left(\frac{|RM|}{10^4 \text{ rad m}^{-2}}\right) \left(\frac{R}{10^{-2} \text{ pc}}\right)^2 \quad (3)$$

where R is the radius of the region that contributes to the PRS and the RM, ζ_e is the electron fraction that generates synchrotron emission in the GHz band which can be approximately given by $\zeta_e \sim \gamma_{\text{obs}} n_e(\gamma_{\text{obs}})/n_{e,0}$, γ_{th} the Lorentz factor defined by $\gamma_{\text{th}}^2 \equiv \int n_e(\gamma) d\gamma / \int [n_e(\gamma)/\gamma^2] d\gamma$ (Bruni et al. 2024), and $n_e(\gamma)$ is the differential distribution of electrons and $n_{e,0}$ is the total electron number density. In particular, for an electron distribution with a thermal and a non-thermal component, γ_{th} would be the typical Lorentz factor separating the two components. Such a predicted scaling has been recently verified by the detection of several more PRSs (Bruni et al. 2024; Ibiq et al. 2024).

The PRS of FRB 20240114A has a flux density of $F_\nu = 46 \mu\text{Jy}$ for VLBA observation. Using the host-galaxy redshift of $z = 0.13$, the specific luminosity of the PRS is $L_\nu \approx 2.2 \times$

$10^{28} \text{ erg s}^{-1} \text{ Hz}^{-1}$. The RM of FRB 20240114A is measured to be $RM \approx 338.1 \text{ rad m}^{-2}$ (Tian et al. 2024). In Fig. 3, we plot the relation between the specific luminosity of the PRS against the RM of known FRBs. We can see that the measurements of the FRBs 20121102A, 20190520B, 20201124A, 20240114A and two other PRS candidates (20181030A-S1 and 20190417A-S) well satisfy the predicted relation. Meanwhile, the observed specific PRS luminosity of FRB 20240114A is close to the value of $\zeta_e \gamma_c (R/10^{-2} \text{ pc})^2 \sim 10$.

6. Conclusions

We summarize our findings below:

- Through VLBA observations at pc-scale resolution, we discovered a compact, continuum source consistent with the position of FRB 20240114A. Its flux density, brightness temperature, and radio luminosity suggest a non-thermal origin, and a negative spectral index as expected from previous lower-frequency/resolution MeerKAT observations. These findings suggest that the source is a PRS associated with FRB 20240114A.
- The radio luminosity and Faraday rotation measure place the PRS in the expected region of the L vs RM theoretical relation, further confirming it and strengthening the case for a nebular origin for the continuum emission associated with some FRBs.
- The host galaxy is a dwarf sub-solar metallicity starburst galaxy with spectral properties which exclude an AGN origin for the PRS.

Further VLBI observations will better characterize the radio spectral shape of this peculiar PRS, eventually providing convincing evidence of the presence of a peak. The latter could further constrain the nebular model, providing information on the plasma energetics.

Acknowledgements. The research leading to these results has received funding from the European Union’s Horizon 2020 programme under the AHEAD2020 project (grant agreement no. 871158). Y.P.Y. is supported by the National Natural Science Foundation of China grant No. 12473047 and the National SKA Program of China (2022SKA0130100). A.R. acknowledge INAF project Supporto Arizona & Italia. We thank the staff of the e-Merlin, in particular Dr. David Williams-Baldwin, for their prompt support and assistance with these observations. e-MERLIN is a National Facility operated by the University of Manchester at Jodrell Bank Observatory on behalf of STFC, part of UK Research and Innovation. The National Radio Astronomy Observatory is a facility of the National Science Foundation operated under cooperative agreement by Associated Universities, Inc. This work made use of the Swinburne University of Technology software correlator, developed as part of the Australian Major National Research Facilities Programme and operated under licence. We thank the staff of LBT Observatory and LBT-Italy, in particular D. Paris, E. Marini, and F. Cusano in obtaining these observations. The LBT is an international collaboration of the University of Arizona, Italy (INAF: Istituto Nazionale di Astrofisica), Germany (LBTB: LBT Beteiligungsgesellschaft), the Ohio State University, representing also the University of Minnesota, the University of Virginia, and the University of Notre Dame.

References

- Ahumada, R., Allende Prieto, C., Almeida, A., et al. 2020, *ApJS*, 249, 3
 Arnouts, S., Cristiani, S., Moscardini, L., et al. 1999, *MNRAS*, 310, 540
 Asari, N. V., Cid Fernandes, R., Stasińska, G., et al. 2007, *MNRAS*, 381, 263
 Baldwin, J. A., Phillips, M. M., & Terlevich, R. 1981, *PASP*, 93, 5
 Bassini, L., Feldmann, R., Gensior, J., et al. 2024, *MNRAS*, 532, L14
 Bertin, E. & Arnouts, S. 1996, *A&AS*, 117, 393
 Bhardwaj, M., Kirichenko, A., & Gil de Paz, A. 2024, *The Astronomer’s Telegram*, 16613, 1
 Bhusare, Y., Maan, Y., & Kumar, A. 2024, *The Astronomer’s Telegram*, 16820,

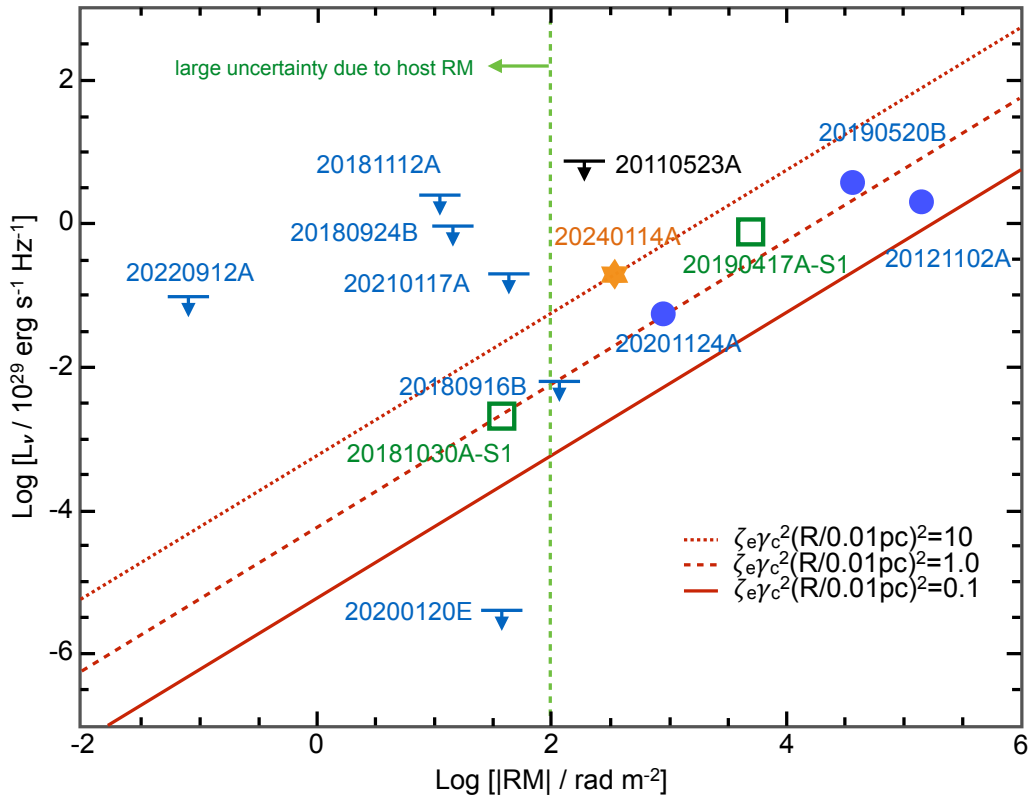


Fig. 3: The proposed relation between the PRS specific radio luminosity and the FRB RM adopting the general nebula model from Yang et al. (2020, 2022). The red dotted, dashed, and solid lines denote the predicted relations for $\xi_e \gamma_c^2 (R/0.01 \text{ pc})^2 = 10, 1.0, 0.1$, respectively. The blue circles denote the FRBs with measured persistent emission flux and RM (FRBs 20121102A, 20190520B and 20201124A). The green squares denote the PRS candidates of 20181030A-S1 and 20190417A-S1 given by Ibik et al. (2024). The black upper limit indicates the non-localized FRB 20110523A with an upper limit of the persistent emission and a measured value of RM, which gives one of the most conservative constraints for non-localized sources in the literature. The blue upper limits correspond to the FRBs with precise (arcsecond) localizations. Owing to the large RM uncertainty of the host interstellar medium, the data of FRBs with $|\text{RM}| \leq (10^2 - 10^3) \text{ rad m}^{-2}$ (on the left side of the green dashed line) might substantially deviate from the predicted relation.

Bochenek, C. D., Ravi, V., Belov, K. V., et al. 2020, *Nature*, 587, 59
 Boquien, M., Burgarella, D., Roehly, Y., et al. 2019, *A&A*, 622, A103
 Bruni, G., Piro, L., Yang, Y.-P., et al. 2024, *Nature*, 632, 1014
 Calzetti, D. 1997, in *American Institute of Physics Conference Series*, Vol. 408, The ultraviolet universe at low and high redshift, ed. W. H. Waller (AIP), 403–412
 CASA Team, Bean, B., Bhatnagar, S., et al. 2022, *PASP*, 134, 114501
 Chambers, K. C., Magnier, E. A., Metcalfe, N., et al. 2016, arXiv e-prints, arXiv:1612.05560
 Chatterjee, S., Law, C. J., Wharton, R. S., et al. 2017, *Nature*, 541, 58
 Curti, M., Cresci, G., Mannucci, F., et al. 2017, *MNRAS*, 465, 1384
 Flewelling, H. A., Magnier, E. A., Chambers, K. C., et al. 2020, *ApJS*, 251, 7
 Fontana, A., Dunlop, J. S., Paris, D., et al. 2014, *A&A*, 570, A11
 Gaia Collaboration, Vallenari, A., Brown, A. G. A., et al. 2023, *A&A*, 674, A1
 Gargiulo, A., Fumana, M., Bisogni, S., et al. 2022, *MNRAS*, 514, 2902
 Giallongo, E., Ragazzoni, R., Grazian, A., et al. 2008, *A&A*, 482, 349
 Ibik, A. L., Drout, M. R., Gaensler, B. M., et al. 2024, *ApJ*, 961, 99
 Ilbert, O., Arnouts, S., McCracken, H. J., et al. 2006, *A&A*, 457, 841
 Kauffmann, G., Heckman, T. M., Tremonti, C., et al. 2003, *MNRAS*, 346, 1055
 Kennicutt, Robert C., J. 1998, *ARA&A*, 36, 189
 Kewley, L. J., Groves, B., Kauffmann, G., & Heckman, T. 2006, *MNRAS*, 372, 961
 Kirsten, F., Marcote, B., Nimmo, K., et al. 2022, *Nature*, 602, 585
 Kirsten, F., Ould-Boukattine, O. S., Herrmann, W., et al. 2024, *Nature Astronomy*, 8, 337
 Margalit, B., Berger, E., & Metzger, B. D. 2019, *ApJ*, 886, 110
 Margalit, B. & Metzger, B. D. 2018, *ApJ*, 868, L4
 Metzger, B. D., Berger, E., & Margalit, B. 2017, *ApJ*, 841, 14
 Moldon, J. 2021, eMCP: e-MERLIN CASA pipeline, Astrophysics Source Code Library, record ascl:2109.006

Murase, K., Kashiyama, K., & Mészáros, P. 2016, *MNRAS*, 461, 1498
 Nicastro, L., Guidorzi, C., Palazzi, E., et al. 2021, *Universe*, 7, 76
 Niu, C. H., Aggarwal, K., Li, D., et al. 2022, *Nature*, 606, 873
 Osterbrock, D. E. 1989, *Astrophysics of gaseous nebulae and active galactic nuclei*
 Piro, L., Bruni, G., Troja, E., et al. 2021, *A&A*, 656, L15
 Pogge, R. W., Atwood, B., Brewer, D. F., et al. 2010, in *Society of Photo-Optical Instrumentation Engineers (SPIE) Conference Series*, Vol. 7735, Ground-based and Airborne Instrumentation for Astronomy III, ed. I. S. McLean, S. K. Ramsay, & H. Takami, 77350A
 Savaglio, S., Glazebrook, K., & Le Borgne, D. 2009, *ApJ*, 691, 182
 Schlafly, E. F. & Finkbeiner, D. P. 2011, *ApJ*, 737, 103
 Schreiber, C., Elbaz, D., Pannella, M., et al. 2018, *A&A*, 609, A30
 Shin, K. & CHIME/FRB Collaboration. 2024, *The Astronomer's Telegram*, 16420, 1
 Snelders, M. P., Bhandari, S., Kirsten, F., et al. 2024, *The Astronomer's Telegram*, 16542, 1
 Tian, J., Rajwade, K. M., Pastor-Marazuela, I., et al. 2024, *MNRAS*, 533, 3174
 Tody, D. 1993, in *Astronomical Society of the Pacific Conference Series*, Vol. 52, *Astronomical Data Analysis Software and Systems II*, ed. R. J. Hanisch, R. J. V. Brissenden, & J. Barnes, 173
 Yang, Y.-P., Li, Q.-C., & Zhang, B. 2020, *ApJ*, 895, 7
 Yang, Y.-P., Lu, W., Feng, Y., Zhang, B., & Li, D. 2022, *ApJ*, 928, L16
 Yang, Y.-P., Zhang, B., & Dai, Z.-G. 2016, *ApJ*, 819, L12
 Zhang, B. 2020, *Nature*, 587, 45
 Zhang, J., Wu, Q., Cao, S., et al. 2024, *The Astronomer's Telegram*, 16505, 1
 Zhang, X. & Yu, W. 2024, *The Astronomer's Telegram*, 16695, 1
 Zhang, Y.-K., Li, D., Zhang, B., et al. 2023, *ApJ*, 955, 142

Appendix A: e-Merlin upper limit

Observations with the enhanced Multi Element Remotely Linked Interferometer Network (e-Merlin) were carried out in five ~ 12 -hour runs between September 20 and 28, 2024, at 5 GHz (C-band), under project CY18016 (PI Bruni). Phase referencing was applied. Visibilities were calibrated through the e-Merlin pipeline (Moldon 2021), and imaged in CASA (CASA Team et al. 2022). An RMS of $10 \mu\text{Jy}/\text{beam}$ was reached, and no source was detected either within the uncertainty region of the FRB coordinates (± 200 mas), or within the wider image field ($20'' \times 20''$). This sets a 5-sigma upper limit of $50 \mu\text{Jy}$ for the candidate PRS flux density at 5 GHz. The image resolution in natural weighting was 228×87 mas.

Appendix B: LBT observations and data reduction

Appendix B.1: MODS spectroscopy

Optical spectroscopy of FRB 20240114A was obtained with the MODS-1 mounted on LBT. Only the MODS-1 arm of the binocular telescope was available during the observations. We employed the dual-grating mode (grisms G400L and G670L) providing a wavelength coverage range 3200–9500 Å, and a slit mask with a width of $1''.2$. Observations were carried on November 10th, 2024 and consisted of three exposures of 1200 s. Slit-alignment was done after blind offsets from a $R \sim 17$ mag star in the field. The slit was centred on the position of the PRS with a North-to-East position angle of $-11:9$, therefore covering only partially the galaxy (Fig. 2).

We processed the spectral data using the Spectroscopic Interactive Pipeline and Graphical Interface (SIPGI) tool, which is specifically designed for the reduction of MODS and LUCI spectra (Gargiulo et al. 2022). We first applied a bad pixels map (generated using imaging flats) to each observed frame, along with a cosmic ray correction. Afterwards, each frame underwent independent bias subtraction and flat-field correction, using a master flat derived from a set of spectroscopic flats. For wavelength calibration, we used the inverse solution of the dispersion, calculated from arc lamp frames and saved in the master lamp. It was then applied to individual frames to calibrate the wavelength and correct for optical distortion. We achieved a wavelength calibration accuracy of $\sim 0.067\text{\AA}$ for the red and $\sim 0.052\text{\AA}$ for the blue channel. Next, we extracted two-dimensional, wavelength-calibrated spectra and performed sky subtraction. To obtain flux-calibrated spectra, we applied the sensitivity function derived from the spectro-photometric standard star Feige 110 observed immediately after the FRB. Finally, the wavelength- and flux-calibrated, sky-subtracted spectra were combined, and the one-dimensional spectrum of each source was extracted.

Figure B.2 shows sections of the spectra around the detected emission lines whose fluxes are reported in Tab. B.1. A redshift of $z = 0.13056 \pm 0.00003$ was determined from the simultaneous detection of the following emission lines: $H\alpha$, $H\beta$, $[\text{N II}] 6585$, $[\text{O II}]$ and $[\text{O III}]$ doublets, $[\text{S II}] 6718$ (see Fig. B.2). Fluxes were measured using the `slinefit`¹ code (Schreiber et al. 2018) which also allows the correction of the Balmer-line fluxes due to the underlying stellar absorption. All the measured fluxes are reported in Tab. B.1. Using the Balmer decrement and assuming the theoretical value for the $(H\alpha/H\beta)$ ratio in the absence of dust, for case B recombination at a gas temperature of 10^4 K (Osterbrock 1989), we derived an intrinsic $A_V = 2.8 \pm 0.3$.

In addition to the $[\text{N II}]/H\alpha$ vs $[\text{O III}]/H\beta$ BPT diagram of Fig. B.3, the location of the source in the $[\text{S II}]/H\alpha$ vs $[\text{O III}]/H\beta$ diagram is shown in Fig. B.4.

Appendix B.2: LBC photometry

Photometric follow-up was obtained in optical with the LBC camera mounted on LBT. Data were obtained in the $g'r'i'z'$ on November 9th, 2024 and additionally in the $r'i'$ on the following night under not excellent sky conditions. LBC imaging data were processed using the data reduction pipeline developed at INAF - Osservatorio Astronomico di Roma (Fontana et al. 2014) which includes bias subtraction and flat-fielding, bad pixel and cosmic ray masking, astrometric calibration, and coaddition. Only the images showing FWHM below $1''.2$ were selected and used, summing up to a total net exposure of 360 s in $g'z'$ -bands, and 1100 and 1200 in $r'i'$ -bands, respectively. Field stars from the GAIA DR3 catalogue (Gaia Collaboration et al. 2023) were used for astrometry calibration. The resulting images average astrometric precision is $0''.05$.

All LBC data were analysed by first performing aperture photometry using DAOPHOT and APPHOT under PyRAF/IRAF (Tody 1993) which was used for the photometric calibration against the *Pan-STARRS* survey (Chambers et al. 2016; Flewelling et al. 2020) for $r'i'z'$ bands and *SDSS DR16* (Ahumada et al. 2020) for g' -band², after careful selection of a set of isolated field stars. For the host-galaxy we applied Petrosian-like elliptical photometry using Source-Extractor (Bertin & Arnouts 1996). It is well detected in all bands and we measure the following AB magnitudes: 22.38 ± 0.05 , 21.86 ± 0.04 , 21.79 ± 0.04 , 21.76 ± 0.10 , respectively in the $g'r'i'z'$ -filters and not corrected for the foreground Galactic extinction. These values are consistent, within errors, with those reported by the *Pan-STARRS* survey. As a cross-check, we downloaded the *SDSS* images and independently measured consistent magnitudes, within errors.

Appendix B.3: SED fitting

After correcting our $u'g'r'i'z'$ data-set for the Galactic foreground extinction of $E(B - V) = 0.06$ mags (Schlafly & Finkbeiner 2011), we modeled the SED of the host galaxy using the code `Cigale`³ (Boquien et al. 2019) with a redshift fixed to $z = 0.13$. The $u' = 23.0 \pm 0.4$ SDSS detection (model magnitude) was added to our dataset. At first, we modeled the SED with a free $E(B - V)_{\text{star}}$, and afterwards we fixed its value and used a derived stellar dust attenuation derived from the one measured with the Balmer decrement, $E(B - V)_{\text{star}} = 0.4 \times E(B - V)_{\text{gas}}$ (Calzetti 1997; Asari et al. 2007). Both modeling gave a similar and well constrained mass of $M_{\star} = 10^{8.1 \pm 0.2} M_{\odot}$. The obtained SFR, attenuation and age are consistent between the two models, but loosely constrained by their large errors. Fixing the metallicity to the value found via spectroscopy did not improve the fit. Figure B.1 shows the best-fit model we obtained and fixed $E(B - V)$. It provides a $\chi^2/\text{dof} = 0.25$ and a star-formation rate $\text{SFR} < 1 M_{\odot} \text{yr}^{-1}$. While the derived stellar mass is reliable, the SFR is degenerate with age (0.3–1.2 Gyr). We found consistent results by modeling the SED with the `LePhare` code (Arnouts et al. 1999; Ilbert et al. 2006). The photometric data are best-fit ($\chi^2/N_{\text{filt}} = 4.9/5$) by a galaxy with the same stellar mass found

² The g' from *Pan-STARRS* does not match exactly the SLOAN filter, though the magnitude offset is smaller than the error.

³ <https://cigale.lam.fr/>

¹ <https://github.com/cschreib/slinefit>

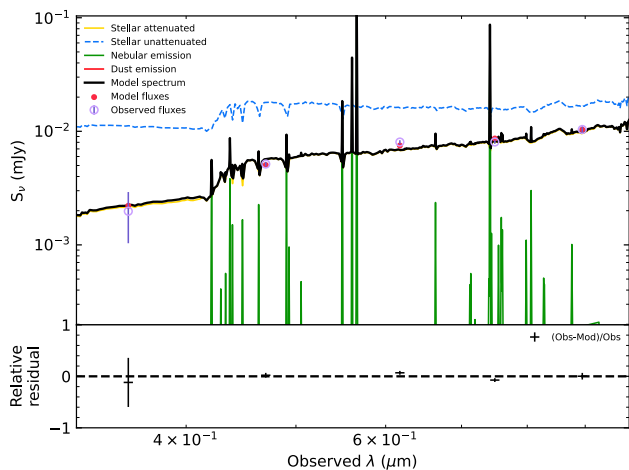


Fig. B.1: SED fitting of the SDSS u' and LBC $g' r' i' z'$ photometry of the host galaxy with Cigale. The best model (solid line) is shown along with the model predicted magnitudes (filled bullets). Photometric measurements are marked by violet empty circles.

Table B.1: Emission lines fluxes and uncertainties in units of 10^{-17} [erg s $^{-1}$ cm $^{-2}$]. Values corrected for Galactic extinction only.

Line	Fluxes
[O II] 3727	4.8 ± 0.4
[O II] 3729	6.4 ± 0.4
H β	2.5 ± 0.4
[O III] 5007	11.2 ± 0.6
[O III] 4959	3.8 ± 0.4
H α	19.8 ± 0.3
[N II] 6549	0.6 ± 0.1
[N II] 6584	2.2 ± 0.3
[S II] 6718	2.9 ± 0.3

above. Also in this case SFR, age and dust-extinction are degenerate and unconstrained.

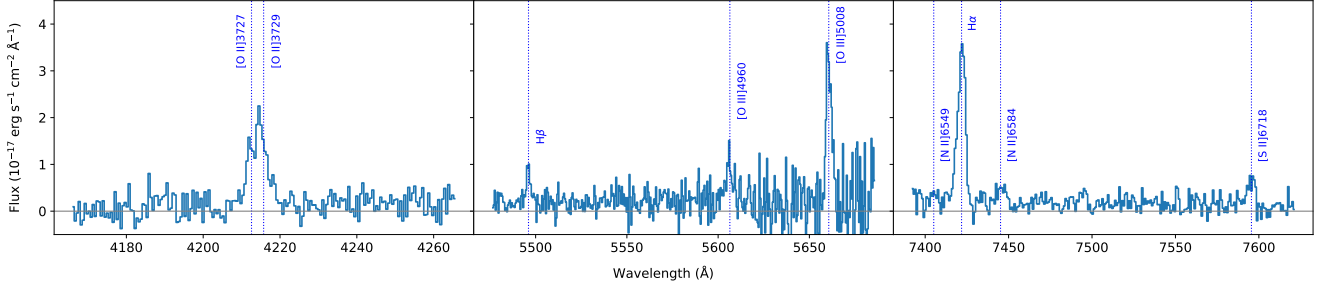


Fig. B.2: Optical emission lines detected with LBT/MODS at the position of the PRS. The three panels show spectral intervals around the lines: the [O II] doublet (left panel); the $H\beta$ and [O III] doublet (central panel); $H\alpha$, [N II] 6549, [N II] 6584, and [S II] 6718 (right panel).

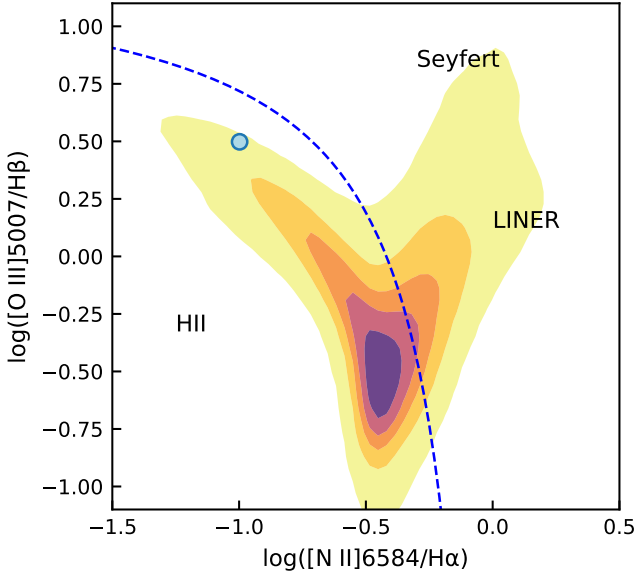


Fig. B.3: BPT empirical optical emission-line diagnostic diagram using the optical line ratios [N II]/ $H\alpha$ and [O III]/ $H\beta$. Shade areas represent the distribution of galaxies with both u' and r' meaningful Petrosian magnitudes in the SDSS catalogue. The dashed line, computed by Kauffmann et al. (2003), delimits the star-forming galaxies region. The FRB host galaxy is marked by a filled circle. Errors are smaller than the marker size.

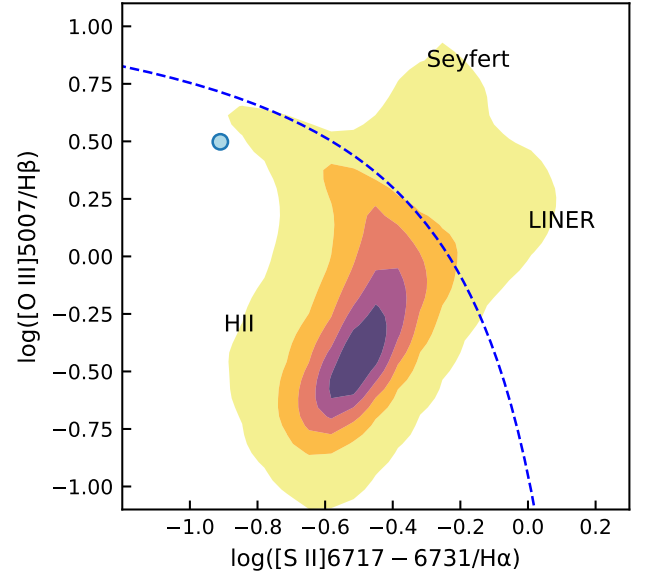


Fig. B.4: BPT diagram showing the ratios [S II]/ $H\alpha$ and [O III]/ $H\beta$. The FRB host galaxy is marked by a filled circle. Errors are smaller than the marker size. Background galaxies were selected from the SDSS catalogue under the condition of having meaningful u' and r' Petrosian-like elliptical aperture magnitudes. The maximum starburst line, computed by Kewley et al. (2006), is shown.